AIAA-95-2007
New High-Order Semi-Implicit Runge-Kutta Schemes for Computing Transient Nonequilibrium Hypersonic Flow

Xiaolin Zhong
University of California, Los Angeles
Los Angeles, CA

29th AIAA Thermophysics Conference
June 19-22, 1995/San Diego, CA

NEW HIGH-ORDER SEMI-IMPLICIT RUNGE-KUTTA SCHEMES FOR COMPUTING TRANSIENT NONEQUILIBRIUM HYPERSONIC FLOW

Xiaolin Zhong *
University of California, Los Angeles, California 90095

Abstract

High-order accurate and efficient numerical methods are required for time-accurate computations of three-dimensional transient nonequilibrium hypersonic flow. There are two major difficulties in such computations: 1), the governing equations are stiff in time integration because nonequilibrium flow has a wide range of time scales; and 2), it is difficult to do high-order computations on hypersonic flow fields involving shock-wave and shock/boundary-layer interaction. In this paper, we propose a new set of high-order semi-implicit Runge-Kutta schemes for integrating nonequilibrium flow equations with stiff source terms. The coefficients of such schemes, which are up to third-order accurate and are strongly A-stable for the stiff terms, have been derived. Meanwhile, we use finite-difference TVD or ENO schemes for high-order multi-dimensional spatial discretization. we have also derived an accurate and efficient approximation method to evaluate vibrational temperature used in the physical model. Finally, the new schemes are tested in several one- and two-dimensional steady and transient nonequilibrium flow problems.

Introduction

This paper concerns with suitable numerical methods for computing three-dimensional transient hypersonic flow associated with maneuvering hypersonic vehicles. These numerical simulations can have many applications in the studies of nonequilibrium hypersonic flows involving unsteady shock-wave/boundary-layer interaction, stability and transition of hypersonic boundary layers, and turbulent hypersonic flows. For such computations, high-order numerical methods are required in order to capture small-scale flow features. Computing transient hypersonic flow is difficult in two aspects: the presence of shock-wave/boundary-layer interaction in the flow fields. and the stiffness of the governing equations in time integration.

*Assistant Professor, Mechanical, Aerospace and Nuclear Engineering Department, Member AIAA.

The existence of shock waves in the flow fields makes it difficult to obtain spatially high-order discretization solutions because of the discontinuous nature of the shock waves. Among current methods, the ENO[1] and TVD[2] schemes can capture shock with high-resolutions, i.e., they are high-order accurate in smooth region of the flow fields, but reduce to first-order accurate inside a shock wave or other discontinuity surfaces. Between the two methods, The TVD schemes are more stable than the ENO schemes in general, on the other hand, the accuracy of the TVD schemes is more limited than the ENO schemes because the local order of accuracy of the TVD schemes reduce to first order at the extremas of the smooth solutions. Therefore, the ENO schemes are more suitable for transient flow simulations, but the TVD schemes are better for obtaining steady-state solutions.

The spatial discretization of the governing equations leads to a set of ordinary differential equations which are usually stiff for nonequilibrium problems. The stiffness of hypersonic flow computations is mainly caused by the chemical and thermal source terms modeling finite-rate nonequilibrium processes, and, in some extent, the transport terms normal to the wall inside a boundary layer. The source terms are stiff because they contain a wide range of time scales, some of which are much smaller than the macroscopic transient flow time scales.

For stiff flow equations, implicit methods are needed to replace the explicit time-stepping methods. Practical implicit methods for multi-dimensional reactive flow calculations include the fractional step method and the semi-implicit method. The fractional step method[3, 4], solves the stiff terms and the nonstiff terms independently. The changes resulting from the separate partial calculations are combined together after each procedure. The time restrictions are removed by using different methods to compute each process, and there is no direct coupling between the individual steps. The drawback of this method is that the temporal accuracy is limited to second-order accurate if a Strang[5] splitting method[6] is used.

For compressible reactive flow, a semi-implicit MacCormack method[7, 8, 9, 6] has been used to compute the chemical source terms implicitly while the fluid terms are computed explicitly. Engquist and Sjogreen[10] computed detonation waves using the TVD

and ENO schemes for the convective part of the equations, and incorporated the source term into the time marching Runge-Kutta schemes by a semi-implicit method. Their third-order schemes are $A(\alpha)$ stable for the stiff source term, when the nonstiff convective term satisfies a CFL condition. In a previous paper[11], a new set of semi-implicit Runge-Kutta methods were derived and analyzed based the general form of implicit Runge-Kutta formulas, which are different from those used in Ref. [10]. Fully implicit and Rosenbrock semi-implicit Runge-Kutta methods of both high-order accurate and strongly A-stable (i.e., $A(\frac{\pi}{2})$ stable)[12] for the implicit terms were derived. The strongly A-stable methods are needed for numerical results to reach correct asymptotic values for very stiff problems. The stability and accuracy of the new schemes were tested in several model problems.

In this paper, we will, 1) discuss the governing equations and physical models for nonequilibrium hypersonic flow without ionization and radiation; 2) present the new semi-implicit Runge-Kutta schemes for computing such flows; 3) present some numerical results obtained by a new three-dimensional finite difference computer code using the proposed numerical methods.

Governing Equations

For nonequilibrium hypersonic flow without ionization and radiation at temperature less than about $9000°K$, we use a 5-species, 17-reaction nonequilibrium air model by Park[13, 14], which is appropriate for air flow at temperature below $9000°K$. The three-dimensional governing equations in Cartesian coordinates are

$$\frac{\partial \mathbf{U}}{\partial t} + \frac{\partial \mathbf{F}_j}{\partial x_j} + \frac{\partial \mathbf{F}_{vj}}{\partial x_j} = \mathbf{W} \tag{1}$$

where

$$\mathbf{U} = \begin{Bmatrix} \rho_1 \\ \vdots \\ \rho_m \\ \rho u_1 \\ \rho u_2 \\ \rho u_3 \\ e \\ e_v \end{Bmatrix}, \quad \mathbf{W} = \begin{Bmatrix} \dot{w}_1 \\ \vdots \\ \dot{w}_m \\ 0 \\ 0 \\ 0 \\ 0 \\ \dot{w}_v \end{Bmatrix} \tag{2}$$

$$\mathbf{F}_j = \begin{Bmatrix} \rho_1 u_j \\ \vdots \\ \rho_m u_j \\ \rho u_1 u_j + p\delta_{1j} \\ \rho u_2 u_j + p\delta_{2j} \\ \rho u_3 u_j + p\delta_{3j} \\ (e+p)\, u_j \\ e_v u_j \end{Bmatrix} \tag{3}$$

$$\mathbf{F}_{vj} = \begin{Bmatrix} j_{1j} \\ \vdots \\ j_{mj} \\ \tau_{1j} \\ \tau_{2j} \\ \tau_{3j} \\ \tau_{jk} u_k - q_j \\ -q_{vj} \end{Bmatrix} \tag{4}$$

where $\mathbf{F}_j$ and $\mathbf{F}_{vj}$ are the inviscid and viscous flux vectors in j-th coordinate direction respectively, and $\mathbf{W}$ is the source term vector due to nonequilibrium thermal and chemical processes.

For computations using body fitted grids, the governing equations can be solved by coordinate transformations.

In the model, translational and rotational modes are assumed to have a single translational-rotational temperature T, and the vibrational modes of all diatomic species are modeled by a single vibrational temperature T_v. The pressure is

$$p = \rho R T = \sum_i^m \rho_i R_i T \tag{5}$$

where R_i is the species specific gas constant. The total energy is

$$e = \sum_{i=1}^m \rho_i c_{vi} T + e_v + \frac{\rho}{2} u_k u_k + \sum_{i=1}^m \rho_i h_i^0 \tag{6}$$

where h_i^0 is the heats of formation, c_{vi}, the specific heat at constant volume is equal to $3R_i/2$ and $5R_i/2$ for monatomic and diatomic species respectively, and the total vibrational energy is

$$e_v = \sum_i^d \rho_i R_i \frac{\theta_{vi}}{e^{\theta_{vi}/T_v} - 1} \tag{7}$$

where the summation is carried out only for diatomic species, which are listed as the first d species. θ_{vi} is the characteristic vibrational temperature.

For flow in the continuum regime, the viscous stresses are modeled using the Navier-Stokes equations:

$$\tau_{ij} = -\mu \left(\frac{\partial u_i}{\partial x_j} + \frac{\partial u_j}{\partial x_i} \right) - \lambda \frac{\partial u_k}{\partial x_k} \delta_{ij} \tag{8}$$

where bulk viscosity is assumed to be zero, i.e, $\lambda = -2\mu/3$. The heat flux vectors are modeled by the Fourier law:

$$q_j = -\kappa \frac{\partial T}{\partial x_j} - \sum_{i=1}^m j_{ik} h_i \tag{9}$$

where κ is the heat conduction coefficients. Since the chemical species in the air has close properties, a binary diffusion model is assumed for mass diffusion:

$$j_{ij} = -\rho D_i \frac{\partial c_i}{\partial x_j} \tag{10}$$

where D_i is the diffusion coefficient.

The detailed models for the viscosity, conductivity, and diffusion coefficients for the mixture of air can be found in Refs. [15, 16, 17, 18].

In the governing equations, $\dot{w}_i$ is the chemical source terms, and $\dot{w}_v$ is the vibrational source term. The reaction equations for the current five-species model of Park[13] are

$$N_2 + M \rightleftharpoons 2N + M \tag{11}$$
$$O_2 + M \rightleftharpoons 2O + M \tag{12}$$
$$NO + M \rightleftharpoons N + O + M \tag{13}$$
$$N_2 + O \rightleftharpoons NO + N \tag{14}$$
$$NO + O \rightleftharpoons O_2 + N \tag{15}$$

where M denotes any of the species. An elementary reaction listed above can be written as

$$AB + M \rightleftharpoons A + B + M \tag{16}$$

The change in the amount of constituent AB in moles per cubic meter is

$$\frac{d[AB]}{dt} = -k_f \left(\frac{\rho_{AB}}{M_{AB}}\right)\left(\frac{\rho_M}{M_M}\right) + k_b \left(\frac{\rho_A}{M_A}\right)\left(\frac{\rho_B}{M_B}\right)\left(\frac{\rho_M}{M_M}\right) \tag{17}$$

where k_f and k_b are forward and backward reaction rates.

The source terms for the vibrational equation equations are

$$\dot{w}_s = Q_{T-V} + Q_{V-D} \tag{18}$$

where Q_{T-V} is the translation-vibration coupling and is modeled by a Landau-Teller model:

$$Q_{T-V} = \rho_s \frac{e_{vs}(T) - e_{vs}(T_v)}{\tau_s} \tag{19}$$

where

$$e_{vs}(T) = \frac{R_s \theta_s}{e^{\theta_{vs}/T} - 1} \tag{20}$$

and τ_s is the relaxation time given by Millikan and White[19]. The vibration-dissociation coupling term Q_{V-D} is modeled as

$$Q_{V-D} = \sum_j \dot{w}_j e_{vs}(T_v) \tag{21}$$

An Approximate Method for Computing T_v

In the computations, the total vibration energy is first obtained by the conservation equations, then the vibrational temperature is computed according to Eq. (7), which leads to

$$e_v = \sum_{i=1}^{m} \rho_i R_i f(T_v, \theta_i) \tag{22}$$

where

$$f(T_v, \theta_{vi}) = \frac{\theta_{vi}}{e^{\theta_{vi}/T_v} - 1} \tag{23}$$

Because θ_{vi} varies for different species, the nonlinear Eq. (23) needs to be solved by an iterative method such as the Newton's method. Such interactive procedure is needed at all grid points at every time step and can be computational expensive.

It is observed that the diatomic molecules in air, N_2, O_2, and NO have close value of θ_{vi} as follows:

	O_2	N_2	NO
$\theta_{vi}\,(^\circ K)$	2270	3390	2740

Therefore, we can assume all diatomic molecules have the same average characteristic vibrational temperature $\overline{\theta_v}$ defined by

$$\overline{\theta_v} = 2800^\circ K \tag{24}$$

to obtain an initial estimate T_{v0} directly. The equations for T_{v0} is

$$e_v = \left(\sum_{i=1}^{m} \rho_i R_i\right) f(T_{v0}, \overline{\theta}) \tag{25}$$

The T_{v0} obtained from the equation above is close to the exact value, a much better approximation can be obtained by a first-order Taylor series around $(T_{v0}, \overline{\theta})$:

$$e_v = \sum_{i=1}^{m} \rho_i R_i \left[f_0 + \left(\frac{\partial f}{\partial \theta_{vi}}\right)_0 (\theta_{vi} - \overline{\theta}) + \left(\frac{\partial f}{\partial T_v}\right)_0 (T_{v1} - T_{v0}) \right] \tag{26}$$

The modified value of vibrational temperature T_{v1} can be calculated from the equation above directly and is taken as the approximate vibrational temperature of the air.

The accuracy of this approximate method can be checked by comparing T_{v1} with the exact T_v. Figures 2 and 3 show comparison of T_{v1}, T_{v0}, and exact T_v of a mixture of air. These figures show that T_{v1} is very good approximation of T_v for all the cases considered.

Characteristic Times of Internal Processes

For a mixture of nonequilibrium air, the internal states are the combinations of many internal rate processes, the time scales of such processes are an important factor in characteristerizing flow regimes. The internal thermal and chemical states can be classified as

equilibrium, nonequilibrium, and frozen states depending on if the relaxation time is much larger than, as the same order of magnitude as, or much smaller than the macroscopic characteristic time of the flow, which is usually measured by a Damköhler number.

For our current five-species model, the vibrational relaxation can be measured by the relaxation time τ_s expressed in the form[19]:

$$\tau_s\, p = \exp[a(T^{-1/3} - b) - 18.42]\ atm - s \qquad (27)$$

where a and b are constants for a given species. We use an average values of a and b to estimate the characteristic vibrational relaxation time.

For an elementary reaction given in Eq. (17), the characteristic time corresponding to the forward reaction is

$$\tau_f\, p = \frac{RT}{k_f} \qquad (28)$$

where R is the universal gas constant. We use this characteristic time to roughly estimate a reaction time scale.

Figure 4 shows τp given by Eq. (19) and Eqs. (11) (15) as a function of temperature. This figure shows that the time scale of internal processes of a nonequilibrium air mixture is about five orders of magnitudes apart. Therefore, nonequilibrium flow system is stiff if the smallest relaxation time is much smaller than the macroscopic flow characteristic time.

Numerical Methods

The governing Eq. (1) is solved by the method of lines using a finite difference upwind scheme developed by Shu and Osher[20] to discretize the equation in space. The viscous flux terms are evaluated by central difference methods, and inviscid terms are evaluated by either ENO or TVD schemes with high-order accuracy in space.

Subsequently, the semi-discrete system of ordinary differential equations is solved by a semi-implicit method, in which, the source terms and flux terms involving normal derivatives are solved implicitly, and the rest of the flux terms are solved explicitly. A new set of semi-implicit Runge-Kutta schemes is proposed for stable and high-order temporal discretization.

Spatial discretization

The presence of strong shock in the flow field requires the use of unwind schemes and nonoscillatory reconstruction in the computations. For high-order ENO or TVD schemes, both finite volume or finite difference method can be used[20, 21, 22].

Since third- or higher-order accurate finite volume method for multidimensional flow is a difficult task for both structured and unstructured grids[21, 22], we choose the finite difference formulation of Shu and Osher[20] for three-dimensional high-order computations.

The finite difference ENO or TVD schemes based on flux were developed by Shu and Osher and can be easily applied to multi-dimensional flow. The inviscid flux terms in the governing equation can be written as

$$\frac{\partial \mathbf{F}_j}{\partial x} \approx \frac{\hat{f}_{j+1/2} - \hat{f}_{j-1/2}}{\Delta x} \qquad (29)$$

where the numerical flux $\hat{f}_{j+1/2}$ approximates, to high-order accuracy, a function $h(x_{j+1/2})$ defined by

$$\mathbf{F}_j(x_j) = \frac{1}{\Delta x}\int_{x-\frac{\Delta x}{2}}^{x+\frac{\Delta x}{2}} h(\xi)d\xi \qquad (30)$$

In the calculations, $h_{j+1/2}$ are reconstructed by a divided difference tables $\mathbf{F}_j$ defined by:

$$h[j,1] = \mathbf{F}_j \qquad (31)$$

$$h[j,k] = h[j+1,k-1] - h[j,k-1] \qquad (32)$$
$$k = (1,\cdots,r)$$

where r is the spatial order of accuracy of the scheme.

For first-order upwind scheme,

$$\hat{f}^{(1)}_{j+1/2} = h[i,1] \qquad (33)$$

where i is equal to j or $j+1$ according to the local characteristic directions for each characteristic field. The average eigenvalues and eigenvectors at the interface $x = x_{j+1/2}$ are evaluated using a Roe average procedure between U_i and U_{i+1}. The Roe average method for nonequilibrium flow derived by Grossman and Cinnella[23].

High-order accuracy in computing flux is achieved by non-oscillatory adaptive interpolation based on TVD or ENO reconstructions. For r-th order method:

$$\hat{f}^{(r)}_{j+1/2} = \hat{f}^{(r-1)}_{j+1/2} + h[i,r-1]\alpha(r,i) \qquad (34)$$

where $\alpha(r,i)$ is defined by

$$\alpha(r,i) = \frac{1}{r!}\frac{d}{dx}\left[(x - x_{i-1/2})\right.$$
$$\left.\cdots(x - x_{i+j-3/2})\right]_{x=x_{i+1/2}} \qquad (35)$$

For finite difference method with a structure grid, $\alpha(r,i)$ can be calculated once and saved in the memory.

For the ENO schemes, the stencil is chosen by comparing the magnitudes of two neighboring flux difference values in order to find the one with smaller magnitude. In order to improve the accuracy of the ENO schemes for smooth solutions, several modifications methods have been proposed for the ENO stencil selection procedure[24]. On the other hand, a second-order TVD scheme with a minmod limiter can be obtained by using a minmod function in stead of choosing

a minimum. These procedures will lead to a TVD or an ENO scheme using Roe average as a building block, which needs entropy correction across sonic points. Shu and Osher use a local Lax-Friedrichs schemes as an entropy correction for the ENO scheme. More details can be found in Ref. [20].

Boundary conditions

The boundary conditions in the free stream and in a supersonic exit are either specified or calculated by an extrapolation method. For inviscid flow computations, characteristic relations are used to compute the flow variables at the wall.

Temporal Discretization

The spatial discretization of the governing flow equations leads to a system of first-order ordinary differential equations,

$$\frac{d\mathbf{U}}{dt} = \mathbf{L}(\mathbf{U}) + \mathbf{W} \tag{36}$$

where $\mathbf{L}(\mathbf{U})$, which is the discretized form of $\frac{\partial \mathbf{F}_j}{\partial x_j} + \frac{\partial \mathbf{F}_{vj}}{\partial x_j}$ terms in Eq. (1), can be regroup as:

$$\mathbf{L}(\mathbf{U}) = \mathbf{L}_1(\mathbf{U}) + \mathbf{L}_2(\mathbf{U}) \tag{37}$$

where $\mathbf{L}_1(\mathbf{U})$ is the non-stiff part of the flux and $\mathbf{L}_2(\mathbf{U})$ is the stiff part of the flux terms which are treated implicitly with the source term.

Therefore, the spatial discretization leads to a system of first-order ordinary differential equations,

$$\frac{d\mathbf{u}}{dt} = \mathbf{f}(\mathbf{u}) + \mathbf{g}(\mathbf{u}) \tag{38}$$

where $\mathbf{u}$ is the vector of discretized flow field variables, $\mathbf{f}$ is the result of the spatial discretization of the terms which can be computed explicitly, and $\mathbf{g}$ is the result of the spatial discretization of the stiff terms which are to be computed implicitly. For simplicity, we assume $\mathbf{f}$ and $\mathbf{g}$ are not explicit functions of the time.

Semi-implicit Runge-Kutta schemes

The Runge-Kutta methods are one-step methods involving intermediate stages to achieve high-order accuracy[12, 25]. In Ref. [11], we considered three versions of r-stage semi-implicit Runge-Kutta methods integrate Eq. (38) by simultaneously treating $\mathbf{f}$ explicitly and $\mathbf{g}$ implicitly.

Method A is:

$$\mathbf{u}^{n+1} = \mathbf{u}^n + \sum_{j=1}^{r} \omega_j \mathbf{k}_j \tag{39}$$

$$\mathbf{k}_i = h\{\mathbf{f}(\mathbf{u}^n + \sum_{j=1}^{i-1} b_{ij}\mathbf{k}_j) + \mathbf{g}(\mathbf{u}^n + \sum_{j=1}^{i-1} c_{ij}\mathbf{k}_j + a_i\mathbf{k}_i)\} \tag{40}$$
$$(i = 1, \cdots, r)$$

where h is the time-step size, and a_i, b_{ij}, c_{ij}, w_j are parameters determined by accuracy and stability requirements. Eq. (41) is a nonlinear equation at every stage of the implicit calculations if $\mathbf{g}$ is a nonlinear function of $\mathbf{u}$. The computations are relatively inefficient, since nonlinear solvers, such as the Newton's method, are required to solve such nonlinear equations, but it has the strongest stability properties among the three methods. Method A of r order accuracy is termed SIRK-rA method.

Method B and C, which are more computationally efficient than method A, is a semi-implicit extension of the Rosenbrock Runge-Kutta method[26],

$$\mathbf{u}^{n+1} = \mathbf{u}^n + \sum_{j=1}^{r} \omega_j \mathbf{k}_j \tag{41}$$

$$\left[\mathbf{I} - ha_i\mathbf{J}(\mathbf{u}^n + \sum_{j=1}^{i-1} d_{ij}\mathbf{k}_j)\right]\mathbf{k}_i = h\{\mathbf{f}(\mathbf{u}^n + \sum_{j=1}^{i-1} b_{ij}\mathbf{k}_j) + \mathbf{g}(\mathbf{u}^n + \sum_{j=1}^{i-1} c_{ij}\mathbf{k}_j)\} \tag{42}$$
$$(i = 1, \cdots, r)$$

Where $\mathbf{J} = \frac{\partial \mathbf{g}}{\partial \mathbf{u}}$ is the Jacobian matrix of the stiff term $\mathbf{g}$, and d_{ij} is an additional set of parameters.

Most of the Rosenbrock methods, which are similar to Eqs. (41) and (42), use a single $a_i = a$ in order to use a single LU decomposition in solving Eq. (42) for all stages[27]. However, LU decomposition is often not possible for multi-dimensional reactive flow problems because of the enormous computer memory requirement involved in the LU decomposition method. Therefore, in this paper, the a_i's are allowed to differ from one another in order to have more flexibility in searching for the optimal parameters in both stability and accuracy.

It can also be shown that the coefficient d_{ij}'s do not have a strong effect on accuracy and stability of the numerical method, they are chosen to reduce computer storage requirement by choosing

Method B: $d_{ij} = 0$
Method C: $d_{ij} = c_{ij}$

Similarly, method B and C are termed SIRK-rB and SIRK-rC methods.

Methods B and C are similar to the implicit methods used in computational fluid dynamics and are much more efficient than the full implicit version. But, for some strongly nonlinear problems, method A is necessary because it is more stable for nonlinear problems than the Rosenbrock semi-implicit Runge-Kutta

method is. Therefore, all three versions of the semi-implicit Runge-Kutta methods were considered and coefficients were derived to be both high-order accurate and strongly A-stable for the implicit terms.

Coefficients in SIRK schemes

The parameters of the semi-implicit Runge-Kutta methods are chosen based on both stability and accuracy requirements with the simultaneous coupling between the explicit and implicit terms. The stability condition for a semi-implicit time-stepping scheme can be analyzed by considering a simplified linear model equation to require that the schemes are strongly A stable for implicit terms as long as the explicit satisfied CFL conditions. The optimal parameters are computationally searched in the semi-implicit Runge-Kutta schemes by simultaneously imposing the stability and accuracy conditions discussed above. For example, for third-order schemes, the parameters are searched for simultaneously satisfying the following conditions:

1. Third-order accuracy;
2. Large stability region for the explicit term;
3. A strong A-stability condition for implicit;
4. $a_i > 0$.

The search results in the following coefficients for SIRK methods:

- First-order (SIRK-1A, -1B, -1C) methods:

$$\omega_1 = 1 \qquad a_1 = 1$$

- Second-order (SIRK-2A, -2B, -2C) methods:

$$\omega_1 = 1/2 \qquad \omega_2 = 1/2$$
$$b_{21} = 1$$

two sets of other parameters:

$$a_1 = 1 - \sqrt{2}/2 \qquad a_2 = 1 - \sqrt{2}/2$$
$$c_{21} = \sqrt{2} - 1$$

or

$$a_1 = 1/4 \qquad a_2 = 1/3$$
$$c_{21} = 5/12$$

- Third-Order SIRK methods:

$$\omega_1 = 1/8 \qquad \omega_2 = 1/8$$
$$\omega_3 = 3/4 \qquad b_{21} = 7/8$$
$$b_{31} = 71/252 \qquad b_{32} = 7/36$$

SIRK-3A:

$$a_1 = .485561 \qquad a_2 = .951130$$
$$a_3 = .189208 \qquad c_{21} = .306727$$
$$c_{31} = .45 \qquad c_{32} = -.263111$$

SIRK-3B:

$$a_1 = 1.40316 \qquad a_2 = .322295$$
$$a_3 = .315342 \qquad c_{21} = 1.56056$$
$$c_{31} = 1/2 \qquad c_{32} = -.696345$$

SIRK-3C:

$$a_1 = .797097 \qquad a_2 = .591381$$
$$a_3 = .134705 \qquad c_{21} = 1.05893$$
$$c_{31} = 1/2 \qquad c_{32} = -.375939$$

where a_1, a_2, a_3, c_{21}, and c_{32} are irrational numbers with six significant digits. The double-precision values of these parameters are listed in Table 1.

The stability of the new SIRK schemes and other semi-implicit schemes were analyzed and tested for several model equations in Ref. [11]. The new methods were found to be stable and high-order accurate in those test cases.

Results

A new three-dimensional high-order finite-difference SIRK inviscid computer code has been written using the numerical methods discussed in this paper. Viscous terms are currently being incorporated in the SIRK code. The code has an option of using either TVD or ENO schemes in spatial discretization. It uses semi-implicit Runge-Kutta method in treating the fluid terms explicitly and the source term implicitly, and it uses five-species air chemistry model of Park and simple Landau-Teller model for vibrational relaxation.

We have computed several inviscid, steady and transient, hypersonic flow problems using the new SIRK code.

Case 1: nonreacting flow in a shock tube

We first tested the new SIRK code in a nonreacting shock tube problem with the following initial conditions:

$$\begin{cases} \rho = 1 kg/m^3 \\ p_1 = 10^5 Pa \end{cases} \quad \text{when} x < 0$$

$$\begin{cases} \rho = 0.01 kg/m^3 \\ p_1 = 10^3 Pa \end{cases} \quad \text{when} x \geq 0$$

The initial species mass fraction are:

$$\begin{aligned} &C_1 = C_{N_2} = 0.79, \quad C_2 = C_{O_2} = 0.21, \\ &C_3 = C_{NO} = 0, \quad C_4 = C_N = 0, \\ &C_5 = C_O = 0 \end{aligned} \tag{43}$$

This flow has a maximum temperature of $700°K$. Therefore the vibrational and chemical modes can be considered frozen, and the gas is a perfect gas. The exact solutions are available for comparison.

Figures 5 to 7 show the comparison of numerical solutions (circles) with analytical solution (lines). The numerical solutions are obtained by the multicomponent SIRK code using the 3rd-order local Lax-Fridrichs ENO (ENO-LLF) scheme and explicit third-order TVD Runge-Kutta schemes of Shu and Osher. The results are consistent with other ENO codes for perfect gas. The use of ENO-LLF scheme produces more numerical dissipation across the shock, and the contact surface compared with ENO schemes is based on Roe flux. The dissipation can be reduced by improving the spatial schemes. Since the emphasis of this paper is on the semi-implicit schemes, we have not fully optimaized the spatial part of the methods.

Case 2: unsteady 1-D nonequilibrium flow

The second case is to use initial shock interaction to create high enough temperature to cause vibrational and chemical excitation between the two shocks (Figure 1). The initial conditions are:

$$\begin{cases} \rho = 3.97 kg/m^3 \\ p = 2.3 \times 10^6 Pa \\ M = 1.5 \end{cases} \quad \text{when} \quad -\frac{L}{2} \geq x < 0$$

$$\begin{cases} \rho = 3.97 \times 10^{-1} kg/m^3 \\ p = 2.3 \times 10^5 Pa \\ M = -1.5 \end{cases} \quad \text{when } 0 \leq x \leq \frac{L}{2}$$

where the length of the computational domain is $L = 10^{-2} m$. The initial mass factions are the same as those of the previous case. The initial non-zero velocity is needed so that high temperature can only be created in the interior of the flow field with a low initial temperature.

In order to capture the relaxation zone behind the shock, both 400 and 800 grid points are used for the present problem. A CFL number of 0.4 based on inviscid characteristic speeds is used for both reacting and nonreacting cases. The numerical solutions are obtained by using the 3rd-order ENO-LLF scheme in space and SIRK-3A method in time. It was found that the third-order semi-implicit methods is several orders of magnitude more stable than the pure explicit methods in terms of allowable time step sizes.

Figures 8 to 12 show the numerical solutions of the nonequilibrium shock interaction problem. The initial discontinuities generate two shock waves and a contact surface moving in the tube. The shock on the right is a strong shock and the shock on the left is a weak one. Figure 9 shows that there is mainly a chemical relaxation zone behind the strong shock and a primarily vibrational relaxation zone following the weak shock. The relaxation zone on the left is much longer than the one on the right. Meanwhile the density and pressure distribution also show the relaxation zones.

Case 3: nonequilibrium shock/entropy wave interaction

As a part of our studies of interaction of free stream disturbances with shock waves[28], we tested the new 3rd order SIRK methods with 3rd-order accurate ENO schemes to the computations interaction of strong shock with incoming disturbance waves. Specificly, we used the numerical results of nonequilibrium flow of Case 2 for the right running shock as initial conditions, and then superimposed the following density disturbances:

$$\begin{cases} \delta\rho = \epsilon\rho_0 \sin[\omega(x - ut)] \\ \delta p = 0 \\ \delta u = 0 \end{cases} \quad \text{when} x > x_0$$

This corresponds to a entropy wave moving with fluid particle velocity. The interaction with the shock will create a combination of an acoustic wave and entropy wave down stream of the shock.

For shock wave with nonequilibrium relaxation, the nonequilibrium real gas effects on the interaction is currently under our investigation. For such flow with oscillation in the smooth solutions, ENO schemes are able to compute them with high order accuracy.

Figures. 13 to 17 are the results of the shock/entropy wave interaction for the right running shock in the previous case. The initial wave is specificed by $\epsilon = 0.2$ and $\omega = 10.01 m_1$. The results show that the nonequilibrium region has very irregular interaction in density and in temperatures. The vibrational temperature has much less oscillation behind the shock compared with the translational temperature. However, the pressure waves which are only linked to acoustic waves are much less influenced by the presence of the relaxation zone.

Case 4: 2-D nonequilibrium hypersonic flow past a cylinder

As a tested of the SIRK method for multidimensional nonequilibrium flow. A test case of hypersonic flow past a cylinder in a partially dissociated nitrogen is computed. This case has been used to test numerical algorithm because there is an experimental bow shock shape for comparison[14, 29].

We test the semi-implicit Runge-Kutta method for inviscid flow problems with the current model. Since TVD schemes are more stable for steady flow computations, we used 2nd-order TVD schemes in space and SIRK-3A in time. The solutions assuming vibrational and chemical frozen were also calculated for comparison.

A uniform 61×61 grid (Figure 18) is used to compute the 2in diameter case of Hornung. The free stream conditions are

$$C_{N_2} = 0.927, \qquad C_N = 0.073$$
$$u_\infty = 5590 m/s, \qquad T_\infty = 1833$$
$$p_\infty = 2910 pa$$

Figures 19 to 21 show the comparison of flow contours between the frozen and nonequilibrium solutions. The perfect gas assumption in the frozen solutions produces much larger bow-shock standoff distance. Meanwhile, the relaxation creates a relaxation zone behind the bow shock, which can be seen in Figures 22 and 23.

Figures 24 to 25 show the distributions of mass fractions and temperatures across the stagnation line. The results show that the flow has a long relaxation length for chemical modes, but it has a much shorter relation for vibrations.

Finally, the density contours are compared with fringe pattern which represents the gradient of density. Though the comparison is not an exact comparison, at least we can see the bow shock produced by nonequilibrium code is roughly the same as the experiment.

Conclusions

In this paper, we have discussed the physical models and numerical methods for conducting direct numerical simulation of 3-D transient nonequilibrium hypersonic flow. In the process, we found that the vibrational temperature used in the model can be evaluated by a simple and efficient new method with accurate results. For high-order multi-dimensional spatial approximation, we use the finite difference TVD or ENO schemes. For time intergation of the stiff equations, we propose a new second- and third-order semi-implicit Runge-Kutta time-stepping schemes which were derived in our previous paper. The new method is tested in several 1-D and 2-D nonequilibrium flow problems. The computations show that the new high-order schemes are robust while maintaining high-order accuracy. As our next steps, we will test the algorithm and the new computer code on viscous and 3-D flow problems, and we will study transient hypersonic flow phenomena

Acknowledgements

This research was supported by AFOSR grant F49620-94-1-0019, with Dr. L. Sakell as the grant monitor.

References

[1] A. Harten, B. Engquist, S. Osher, and S. Chakravarthy. Uniformly high order accurate essentially non-oscillatory schemes, III. *Journal of Computational Physics*, 71(2), August 1987.

[2] A. Harten. High resolution schemes for hyperbolic conservation laws. *J. of Comp. Phys.*, 49:357–393, 1983.

[3] N. N. Yanenko. *The Method of Fractional Steps.* Springer-Verlag, 1971.

[4] E. S. Oran and J. P. Boris. *Numerical Simulation of Reactive Flow.* Elsevier Science Publishing Co., New York, 1987.

[5] G. Strang. On the construction and comparison of difference schemes. *SIAM Journal of Numerical Analysis*, 5:506–517, September 1968.

[6] R. J. Leveque and H. C. Yee. A study of numerical methods for hyperbolic conservation laws with stiff source terms. *J. of Computational Physics*, 86:187–210, 1990.

[7] T. R. A. Bussing and E. M. Murman. A finite volume method for the calculation of compressible chemically reacting flows. *AIAA Paper 85-0296*, 1985.

[8] J. P. Drummond, R. C. Rogers, and M. Y. Hussaini. Spectral methods for modeling supersonic chemically reacting flow fields. *AIAA Paper 85-0302*, 1985.

[9] H. C. Yee and J. L. Shinn. Semi-implicit and fully implicit shock capturing methods for hypersonic conservation laws with stiff source terms. *AIAA Paper 87-1116*, 1987.

[10] B. Enquist and B. Sjogreen. Robust difference approximations of stiff inviscid detonation waves. Report 91-03, CAM, March 1991. Department of Mathematics, University of California, Los Angeles.

[11] X. Zhong. Semi-implicit Runge-Kutta schemes for direct numerical simulation of transient high-speed reactive flows. *Submitted to Journal of Computational Physics*, 1994.

[12] J. D. Lambert. *Computational Methods in Ordinary Differential Equations.* John Wiley & Sons, 1973.

[13] C. Park. On convergence of chemically reacting flows. *AIAA Paper 85-0247*, 1985.

[14] G. Candler. On the computation of shock shapes in nonequilibrium hypersonic flows. AIAA Paper 89-0312, 1989.

[15] F. G. Blottner. Finite difference methods of solution of the boundary-layer equations. *AIAA J.*, 8:193–205, 1970.

[16] C. R. Wilke. A viscosity equation for gas mixture. *J. of Chemical Physics*, 14(4):517–519, 1950.

[17] J. N. Moss, G. Bird, and V. K. Dogra. Non-equilibrium thermal radiation for an aeroassist flight experiment. AIAA Paper 88-0081, AIAA, 1988.

[18] Graham V. Candler. *The computation of weakly ionized hypersonic flows in thermo-chemicalnonequilibrium.* PhD thesis, Stanford University, 1988.

[19] R. C. Millikan and D. R. White. Systematics of vibrational relaxation. *J. of Chemical Physics*, 39(12):3209–3213, 1963.

[20] C.-W. Shu and S. Osher. Efficient implementation of essentially non-oscillatory schemes II. *Journal of Computational Physics*, 83:32–78, 1989.

[21] T.J. Barth and P.O. Frederickson. Higher order solution of the Euler equations on unstructured grids using quadratic reconstruction. AIAA Paper 90-0013, January 1990.

[22] J. Casper. *Essentially Non-Oscillatory Shock Capturing Schemes to Multi-Dimensional Systems of Conservation Laws.* PhD thesis, Old Dominion University, December 1990.

[23] B. Grossman and P. Cinnella. Flux-split algorithms for flows with non-equilibrium chemistry and vibrational relaxation. *Journal of Computational Physics*, 88:131–168, 1990.

[24] Chi-Wang Shu. Numerical experiments on the accuracy of ENO and modified ENO schemes. *Journal of Scientific Computing*, 5:127–149, June 1990.

[25] J. C. Butcher. Implicit Runge-Kutta processes. *Math. Comp.*, 18:50–64, 1964.

[26] H. H. Rosenbrock. Some general implicit processes for the numerical solution of differential equations. *Comput. J.*, 5:329, 1963.

[27] P. Kaps and P. Rentrop. Generalized Runge-Kutta methods of order four with stepsize control for stiff ordinary differential equations. *Nummer. Math.*, 33:55–68, 1979.

[28] C.-H. Chiu and X. Zhong. Simulation of transient hypersonic flow using the ENO schemes. 1 1995. AIAA paper 95-0469, 31st AIAA Aerospace Sciences Meeting and Exhibit, Reno, NV, will be submitted to AIAA Journal.

[29] H. G. Hornung. Non-equilibrium dissociating nitrogen flow over spheres and circular cylinders. *Journal of Fluid Mechanics*, 53:149–176, 1972.

Table 1: **The double-precision values of the parameters for the SIRK-3 methods**

SIRK-3A:	
$a_1 = .4855612330925677$	$a_2 = .9511295466999914$
$a_3 = .1892078709825326$	$c_{21} = .3067269871935408$
$c_{31} = .45$	$c_{32} = -.2631108321468882$
SIRK-3B:	
$a_1 = 1.403160446775581$	$a_2 = .3222947153259484$
$a_3 = .3153416455775987$	$c_{21} = 1.560563684998894$
$c_{31} = \frac{1}{2}$	$c_{32} = -.6963447867610024$
SIRK-3C:	
$a_1 = .7970967740096232$	$a_2 = .5913813968007854$
$a_3 = .1347052663841181$	$c_{21} = 1.058925354610082$
$c_{31} = \frac{1}{2}$	$c_{32} = -.3759391872875334$

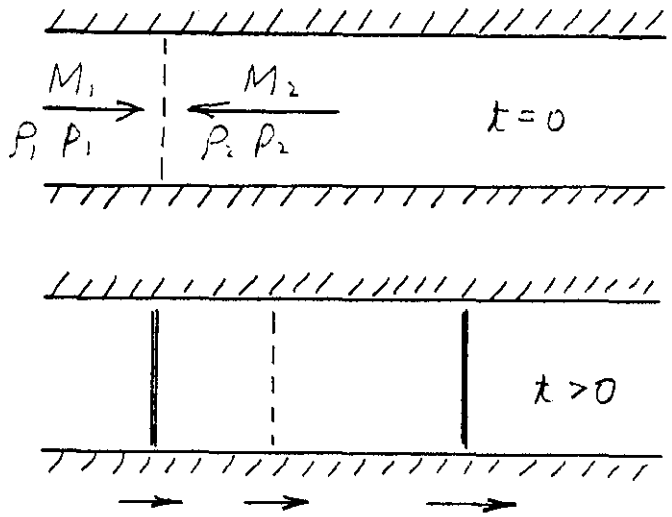

Figure 1: **A schematic of flow field of Case 2.**

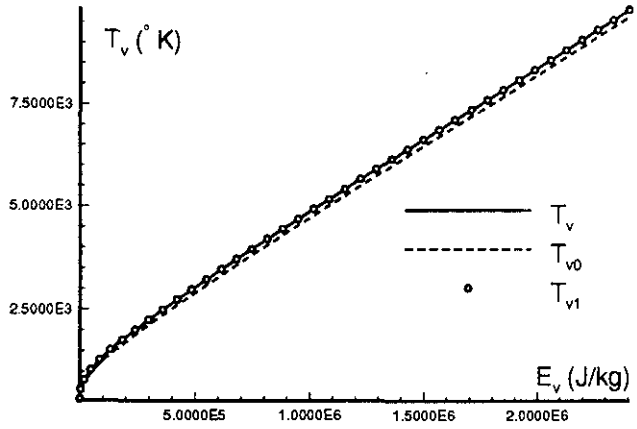

Figure 2: **Approximate and exact vibrational temperatures for air. Mass fractions are** $N_2 : O_2 : NO = 0.79 : 0.21 : 0$.

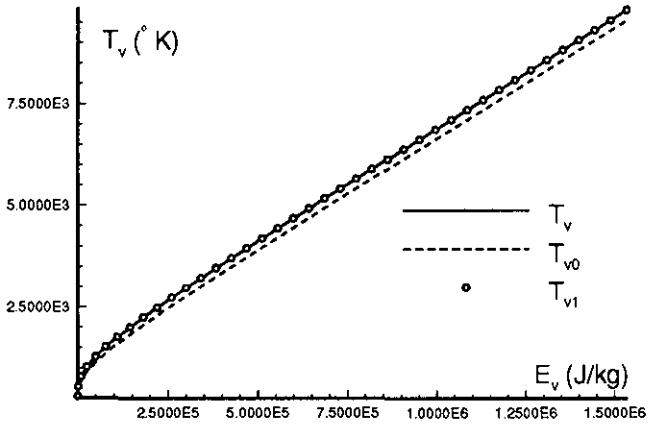

Figure 3: **Approximate and exact vibrational temperatures for air. Mass fractions are:** $N_2 : O_2 : NO = 0.6 : 0 : 0.03$.

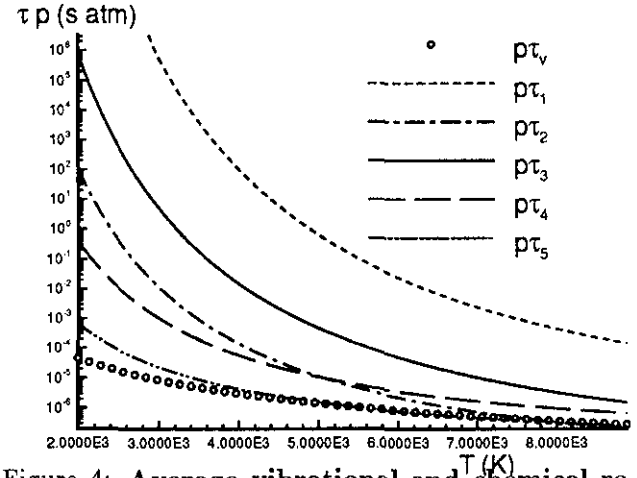

Figure 4: **Average vibrational and chemical relaxation times of the five-species air model of Park.**

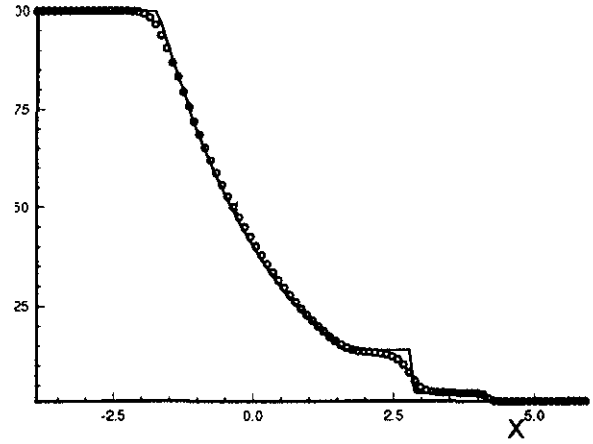

Figure 5: **Density distribution of nonreacting shock tube flow using the 3rd-order ENO-LLF scheme.**

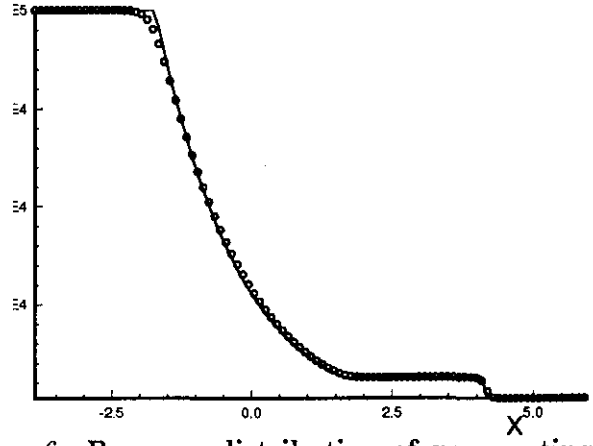

Figure 6: **Pressure distribution of nonreacting shock tube flow using the 3rd-order ENO-LLF scheme.**

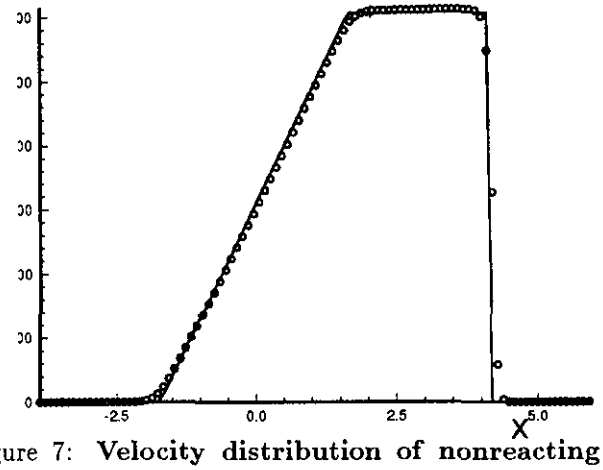

Figure 7: **Velocity distribution of nonreacting shock tube flow using the 3rd-order ENO-LLF scheme.**

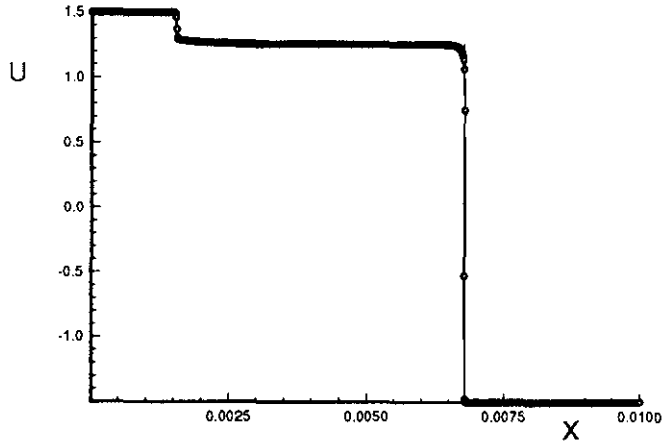

Figure 8: **Velocity distribution of a reacting shock interaction (SIRK-3A with 3rd-order ENO-LLF scheme).**

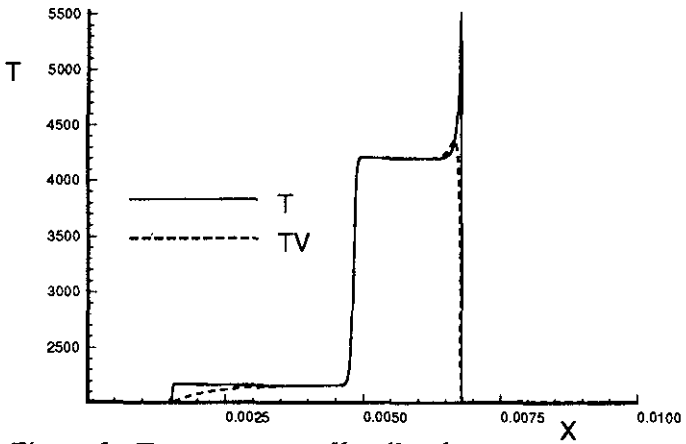

Figure 9: **Temperature distributions of a reacting shock interaction (SIRK-3A with 3rd-order ENO-LLF scheme).**

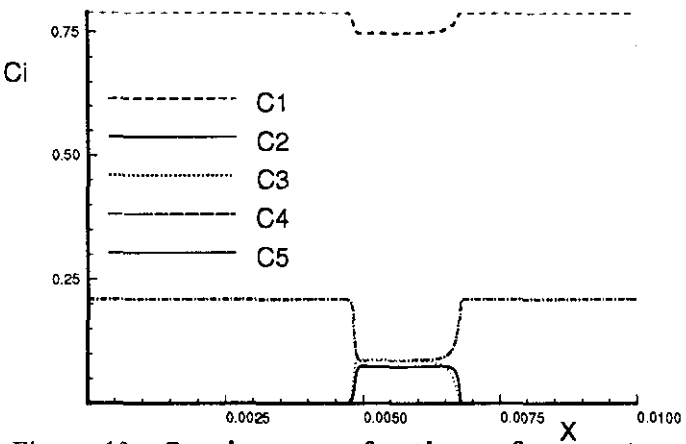

Figure 10: **Species mass fractions of a reacting shock interaction (SIRK-3A with 3rd-order ENO-LLF scheme).**

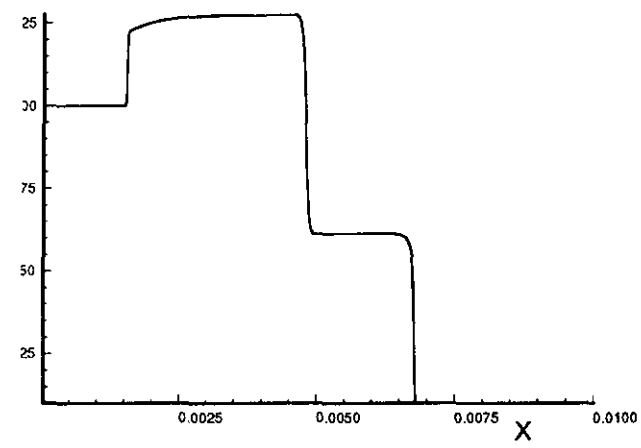

Figure 11: **Density distributions of a reacting shock interaction (SIRK-3A with 3rd-order ENO-LLF scheme).**

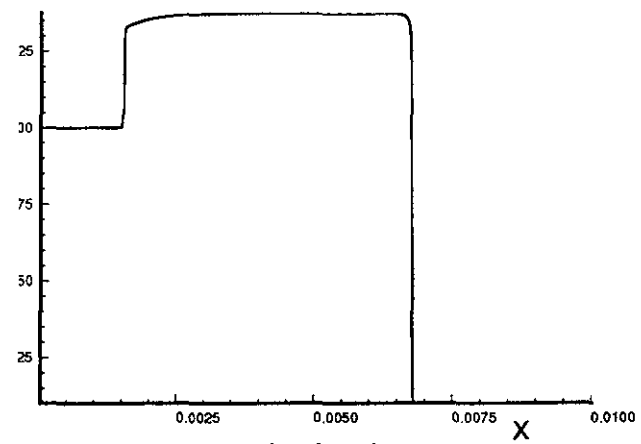

Figure 12: **Pressure distributions of a reacting shock interaction (SIRK-3A with 3rd-order ENO-LLF scheme).**

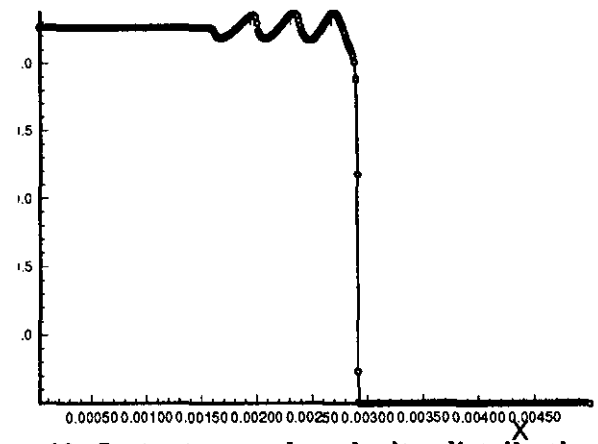

Figure 13: **Instantaneously velocity distribution of incoming entropy wave interaction the right runing reacting shock wave.**

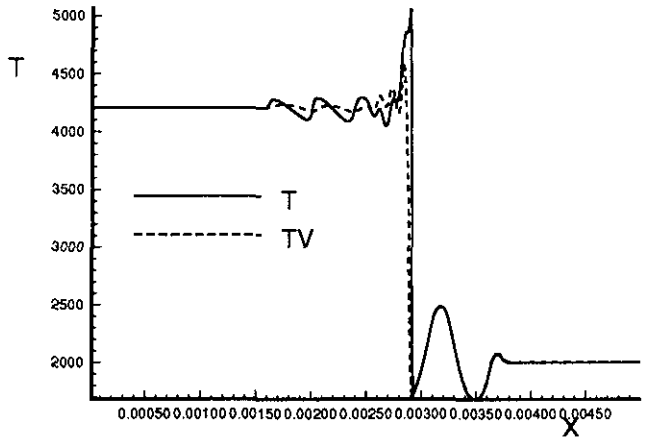

Figure 14: **Instantaneously temperature distributions of incoming entropy wave interaction the right runing reacting shock wave.**

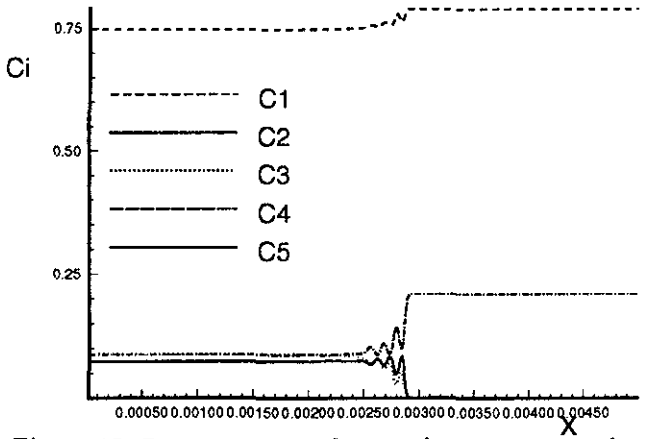

Figure 15: **Instantaneously species concentration distributions of incoming entropy wave interaction the right runing reacting shock wave.**

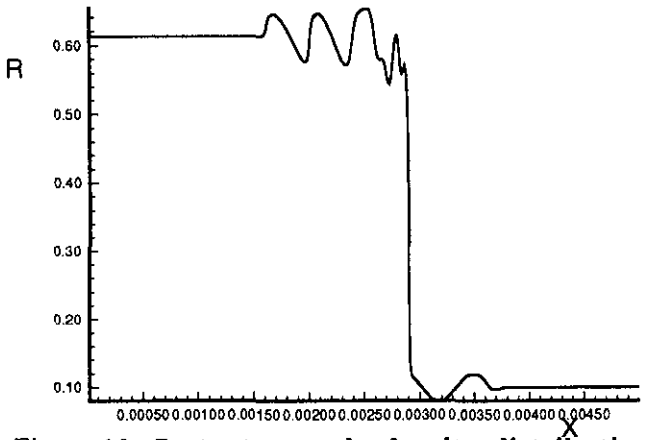

Figure 16: **Instantaneously density distribution of incoming entropy wave interaction the right runing reacting shock wave.**

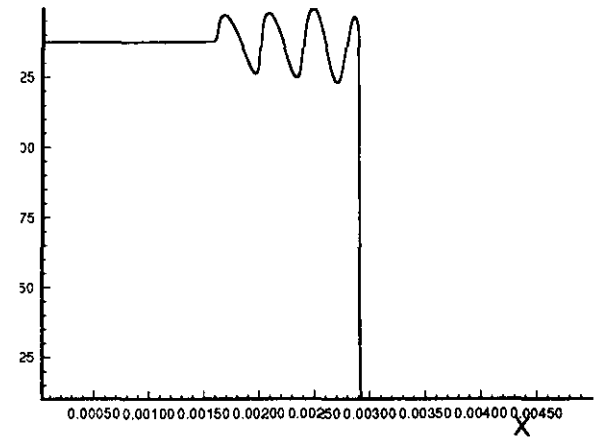

Figure 17: **Instantaneously pressure distribution of incoming entropy wave interaction the right runing reacting shock wave.**

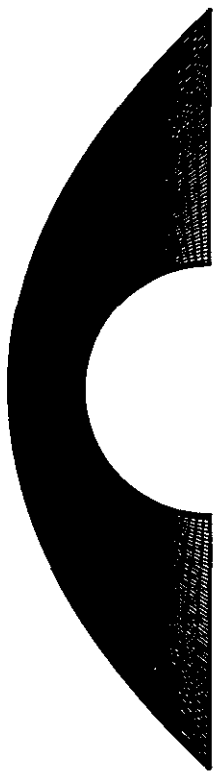

Figure 18: **Computational grid for case 4.**

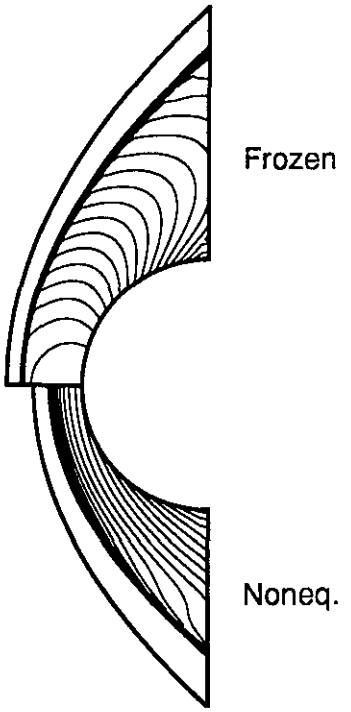

Figure 19: **Translational temperature contours of frozen and nonequilibrium flow solutions.**

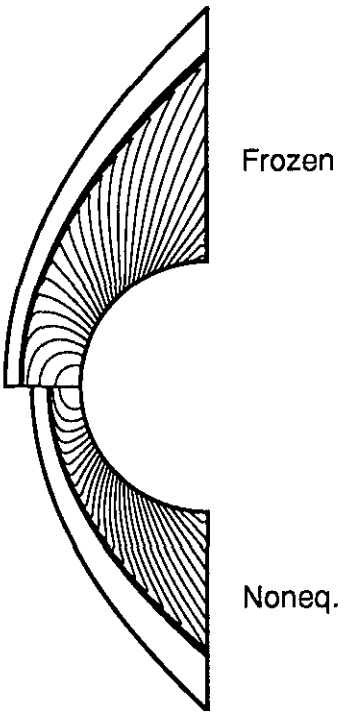

Figure 20: **Pressure contours of frozen and nonequilibrium flow solutions.**

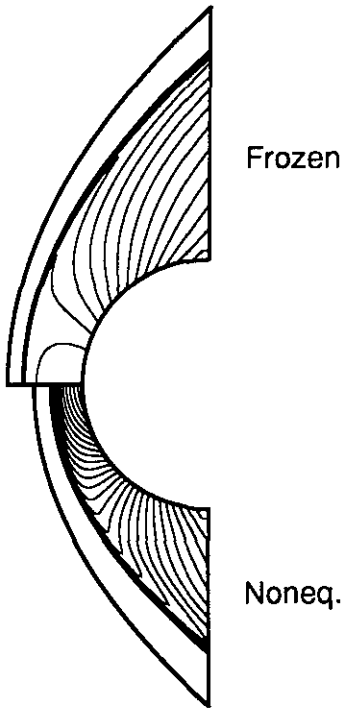

Figure 21: **Density contours of frozen and nonequilibrium flow solutions.**

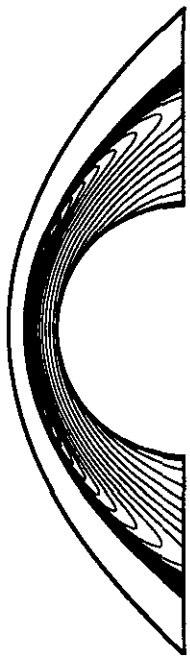

Figure 22: **Vibrational temperature contours of reacting flow solutions.**

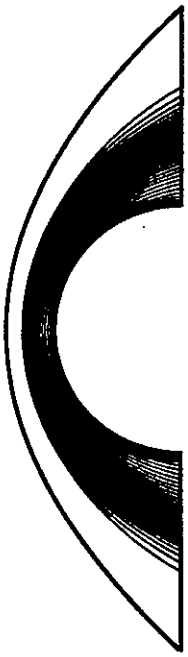

Figure 23: **Mass Fraction N_2 contours of nonequilibrium flow solutions.**

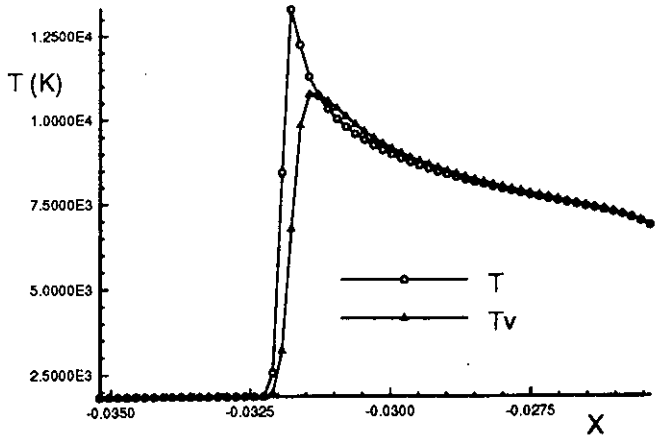

Figure 25: **Temperature distributions of the nonequilibrium solutions along the stagnation line.**

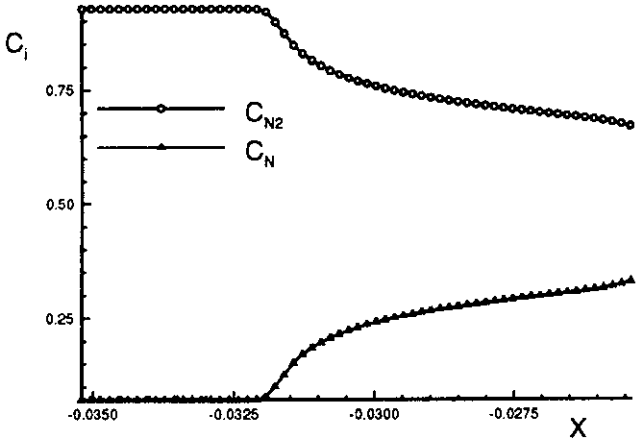

Figure 24: **Species mass fraction distributions of the nonequilibrium solutions along the stagnation line.**

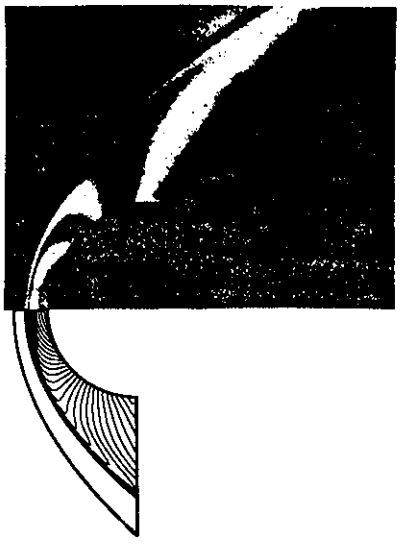

Figure 26: **Density contours of nonequilibrium solutions and Hornung's experimental fringe patterns**